Flexible Microwave Waveforms Synthesis Based on Wavelength Sensitive Bias Shift of a Mach–Zehnder Modulator

Xiaohong Lan [ID], Yang Jiang [ID], Yuejiao Zi [ID], Xiangping Chen, Qiang Yu [ID], Jiahui Li [ID], and Na Chen

Abstract—A new scheme of arbitrary microwave waveform generation based on one single-drive Mach–Zehnder modulator (MZM) is proposed. Due to the characteristic of the wavelength-dependent bias shift in a MZM, two light fields with different wavelength can carry two sets of modulation components and contribute the desired waveforms through both of the Fourier synthesis and time-domain synthesis. Thanks to plentiful and controllable harmonics generation, some challenging waveforms generation, such as parabolic waveform, sawtooth waveform and frequency doubling triangular waveform, can be achieved, which are verified by the theoretical analysis and experimental results. This method exhibits not only more flexible waveform generation ability, but also the advantages of simple configuration, easy operation and high efficiency of bandwidth utilization.

Index Terms—Mach–Zehnder modulator, microwave waveform generation, microwave photonics.

I. INTRODUCTION

MICROWAVE arbitrary waveforms are widely applied to radar, wireless communication and signal processing, etc [1]–[4]. In general, microwave waveforms are generated by electronic system, but the limited bandwidth makes the signal generation with high frequency difficult to be obtained. Fortunately, photonic technologies provide new solutions for the task due to the advantages of large bandwidth, anti-electromagnetic interference, low loss and so on.

The typical photonic method for arbitrary waveform generation is Fourier synthesis. Starting from an optical frequency comb, the amplitude and phase of each spectral line are manipulated by a spatial phase modulator, and the desired waveform can be achieved after photoelectric detection [5]. Although this technique is effective and powerful, the complex configuration and environmental perturbation affects the practicability. To conveniently and accurately obtain the required frequency components, the technique of external modulation is a good choice because the amplitude and phase of each modulation tone can be strictly controlled [6]–[11]. By this means, there are many successful demonstrations of triangular, sawtooth or rectangular waveforms generation, in which the cascaded single-drive Mach–Zehnder modulator (MZM), dual-drive MZM or dual-parallel MZM are employed [12]–[14]. Even so, such schemes do not come up to expectations. The first reason is that the number of the modulation harmonics is always limited and the relationship among harmonics can not fit for arbitrary Fourier synthesis requirement. It greatly obstructs the diversity and accuracy of generated waveforms. Secondly, the advanced modulators, such as dual-drive MZM or dual-parallel MZM, usually increase the system cost and operation complexity.

Time-domain synthesis is another effective way to generate desired waveforms. In this method, the wanted signals can be achieved by carving and overlapping the signal envelopes in time domain [12], [15]–[17], where the modulator implements the envelope graver. This technique avoids the optical spectral line manipulation, but the operation bandwidth is greatly limited by the bandwidth of modulator.

In fact, arbitrary waveform generation can be more effectively realized by comprehensive utilization of Fourier synthesis and time-domain synthesis [18]–[20], where the external modulation is a universal technique. Considering that a single-drive MZM is the simplest modulator, how to sufficiently utilize the bandwidth and generate more plentiful harmonics form single-drive MZM is a significant work.

In this paper, a novel scheme of arbitrary waveform generation based on one single-drive MZM and two optical carriers is proposed. As we know, under certain bias voltage, the corresponding bias point of a MZM is wavelength dependent [21], which means two optical carriers with different wavelengths can contribute two sets of modulation sidebands through one MZM. By taking the advantages of Fourier synthesis and time-domain synthesis, the desired waveforms can be obtained by manipulating and superposing these two optical fields without assistant spectral line filtering. Theoretical analysis shows that the scheme can deeply exploit the harmonics generation capability of a MZM, and flexible waveforms can be consequently generated. From the experimental demonstration, besides sawtooth (or

Xiaohong Lan, Yang Jiang, Xiangping Chen, Qiang Yu, Jiahui Li, and Na Chen are with the Department of Physics, College of Physics, Guizhou University, Guiyang 550025, China (e-mail: gs.xhlan20@gzu.edu.cn; jiangy@gzu.edu.cn; gs.xpchen19@gzu.edu.cn; gs.yuq19@gzu.edu.cn; gs.jiahuili20@gzu.edu.cn; gs.chenn20@gzu.edu.cn).

Yuejiao Zi is with the Department of Electric Science and Technology, College of Big Date and Information Engineering, Guizhou University, Guiyang 550025, China (e-mail: gs.yjzi16@gzu.edu.cn).
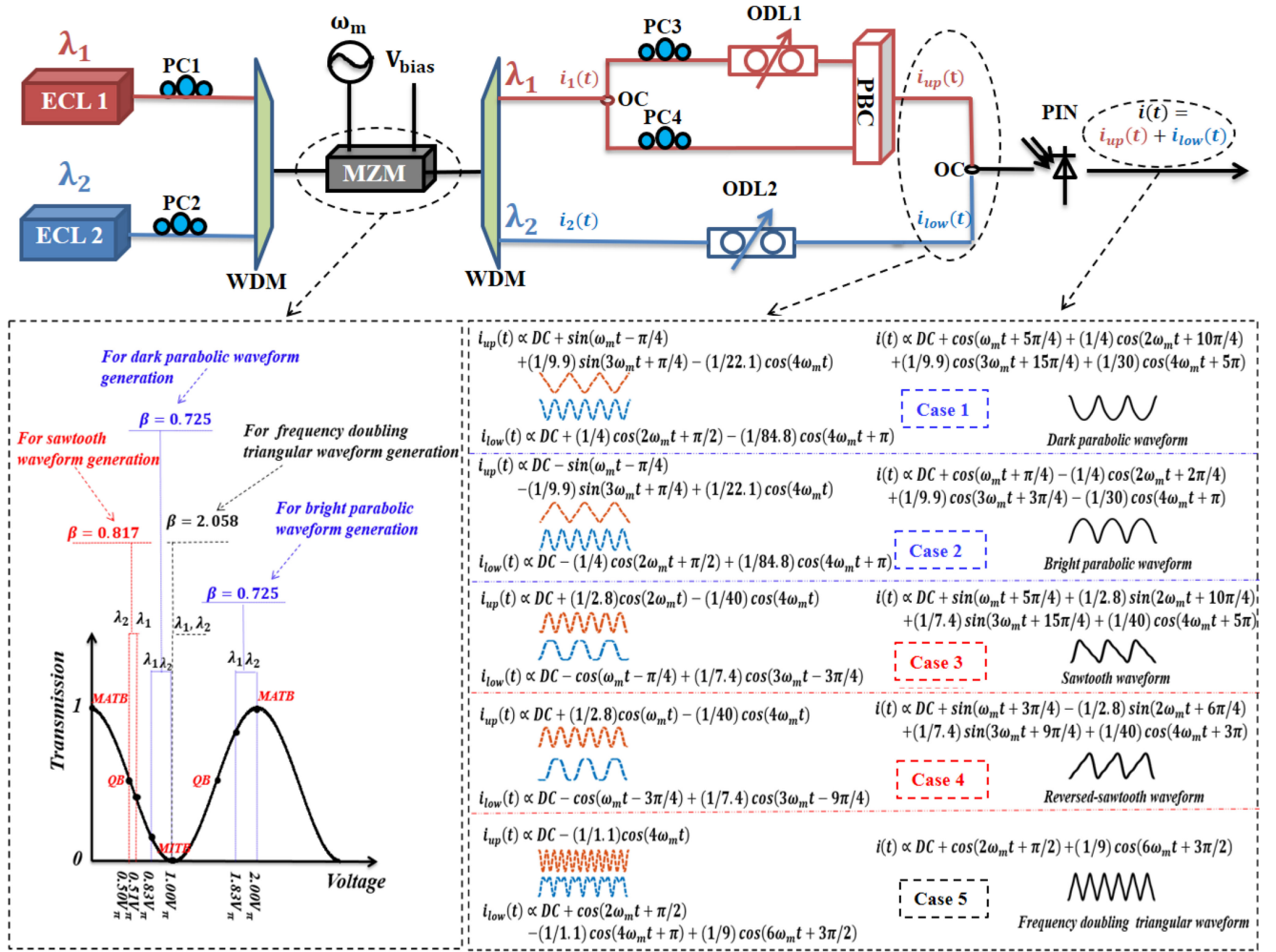
Fig. 1. Configuration and diagrammatic presentation of the proposed microwave waveform generator. ECL: external cavity tunable laser, PC: polarization controller, WDM: wavelength division multiplexer, MZM: Mach–Zehnder modulator, OC: optical coupler, ODL: optical delay line, PBC: polarization beam combiner, MATB: Maximum Transmission Bias point, QB: Quadrature Bias point, MITB: Minimum Transmission Bias point.

reversed-sawtooth) waveform, parabola and frequency doubling triangular waveforms are also successfully achieved, which agrees with the theoretical expectation well and exhibits great potential for waveform generation with only one single-drive MZM.

II. OPERATION PRINCIPLE

The diagram of the proposed microwave waveform generator is shown by Fig. 1. When two light fields with wavelength of λ_1 and λ_2 are coupled and launched into MZM, two different sets of modulation sidebands will be produced independently on two light fields because the corresponding bias point is wavelength dependent. After a demultiplexer, λ_1 and λ_2 are separated into the upper branch and lower branch, where the part of required Fourier components can be achieved by manipulating two optical fields respectively. When the pre-processed signals on two branches are recombined, the overlapped envelopes will contribute the signals we want. Now, let's consider the general description of the modulation process in a MZM. If a continuous wave with angular frequency of ω_0 is modulated

by a sinusoidal signal $V(t) = V_m \cos(\omega_m t)$ via a MZM with a dc-bias voltage of V_{bias}, where V_m and ω_m are the amplitude and angular frequency of the drive signal, the output field can be expressed as

$$Eout = E_0 \cos \left[\varphi + \frac{\pi V(t)}{2V_\pi} \right] \cos(\omega_0 t) \tag{1}$$

where E_0 is the optical field amplitude, $\varphi = \pi V_{bias}/(2V_\pi)$ is the bias index related to V_{bias}, and V_π is the half-wave voltage of the MZM. By applying Jacobi Anger expansion to (1), it can be written as

$$
\begin{aligned}
E_{out} = E_0 \cos(\omega_0 t)\{&\cos \varphi J_0(\beta) \\
&+ 2 \sum_{k=1}^{\infty} (-1)^k \cos \varphi J_2 k(\beta) \cos(2k\omega_m t) \\
&+ 2 \sum_{k=0}^{\infty} (-1)^{k+1} \sin \varphi J_2 k+1(\beta) \cos[(2k+1)\omega_m t)]\}
\end{aligned}
$$

$$\tag{2}$$

where J_k is the first kind Bessel function of order k, and $\beta = \pi V_m/(2V_\pi)$ denotes modulation index. According to (2), modulation process results in many spectral lines with frequency space of ω_m, whose amplitudes are determined by β and φ. Because the higher order Bessel functions give the smaller values, only the fourth order approximation is taken into account. Therefore, the modulated optical field is simplified as

$$
\begin{aligned}
E_{out} = E_0 \cos(\omega_0 t)\{ &J_0(\beta)\cos\varphi \\
&- 2J_1(\beta)\sin\varphi\cos(\omega_m t) - 2J_2(\beta)\cos\varphi\cos(2\omega_m t) \\
&+ 2J_3(\beta)\sin\varphi\cos(3\omega_m t) + 2J_4(\beta)\cos\varphi\cos(4\omega_m t)\}
\end{aligned}
\tag{3}
$$

and the corresponding photocurrent can be written as

$$
\begin{aligned}
i_{out}(t) \propto &\, DC + A\cos(\omega_m t) + B\cos(2\omega_m t) + C\cos(3\omega_m t) \\
&+ D\cos(4\omega_m t) + E\cos(5\omega_m t) + F\cos(6\omega_m t)
\end{aligned}
\tag{4}
$$

where the coefficients of each component are

$$
\begin{aligned}
A = &-4J_0 J_1 \sin\varphi\cos\varphi + 4J_1 J_2 \sin\varphi\cos\varphi \\
&- 4J_2 J_3 \sin\varphi\cos\varphi + 4J_3 J_4 \sin\varphi\cos\varphi;
\end{aligned}
$$

$$
\begin{aligned}
B = &-4J_0 J_2 \cos^2\varphi - 4J_2 J_4 \cos^2\varphi \\
&+ 2J_1^2 \sin^2\varphi - 4J_1 J_3 \sin^2\varphi;
\end{aligned}
$$

$$
\begin{aligned}
C = &\, 4J_0 J_3 \sin\varphi\cos\varphi + 4J_1 J_2 \sin\varphi\cos\varphi \\
&- 4J_1 J_4 \sin\varphi\cos\varphi;
\end{aligned}
$$

$$
D = 4J_0 J_4 \cos^2\varphi + 2J_2^2 \cos^2\varphi - 4J_1 J_3 \sin^2\varphi;
$$

$$
E = -4J_2 J_3 \sin\varphi\cos\varphi - 4J_1 J_4 \sin\varphi\cos\varphi;
$$

$$
F = -4J_2 J_4 \cos^2\varphi + 2J_3^2 \sin^2\varphi.
$$

Among the coefficients above, we can find that

$$
A/C = (-J_0 J_1 + J_1 J_2 - J_2 J_3 + J_3 J_4)/(J_0 J_3 + J_1 J_2 - J_1 J_4)
\tag{5}
$$

which indicates that the coefficient ratio between A and C is decided by the modulation index β only, but independent on the bias index φ. It is noted that (5) is established under the condition that it is not biased at MATB or MITB.

A. Parabolic Waveform

Mathematically, the Fourier series expansion of a parabolic waveform $T_{pa}(t)$ is given by

$$
T_{pa}(t) = DC + \sum_{n=1,2,3}^{\infty} \frac{1}{n^2} \cos(n\omega_m t).
\tag{6}
$$

Under the fourth-order approximation, the power ratio exists a tolerance range, which implies that the first four order coefficients exactly obeying the expansion may not be the best option. The comparison result is shown by Fig. 2(a). Because the lower order Fourier component has the larger weight, varying the coefficient of the lower order component
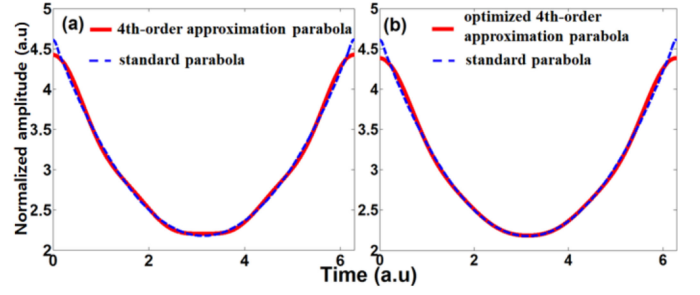

Fig. 2. Comparison results of, (a) 4th-order approximation parabola and standard parabola, (b) Optimized 4th-order approximation parabola and standard parabola.

may give more influence on the waveform. Therefore, by comparing with the standard waveform, one can try to adjust the coefficient of the lowest order component to observe the variation tendency of the approximation waveform to approach the standard waveform. Then, by adjusting the coefficients of the second-order component, third-order component and fourth-order component in sequence, a set of coefficients can be finally tried out to match the standard waveform better. Thus, an optimized parabolic waveform is able to be approached, which can be given by (7),

$$
\begin{aligned}
T_{dark-pa}(t) = &\, DC + \cos(\omega_m t) + (1/4)\cos(2\omega_m t) \\
&+ (1/9.9)\cos(3\omega_m t) + (1/30)\cos(4\omega_m t)
\end{aligned}
\tag{7}
$$

and the comparison result is shown by Fig. 2(b). Clearly, the parabolic waveform defined by (7) matches the standard parabola better. In order to further evaluate the fitting degree of the generated waveform to the standard waveform, we introduce the concept of goodness of fit in statistics. This concept can be defined as the fitting degree between the regression line and observed value, which is given by R-squared (R^2) as below.

$$
R^2 = 1 - \frac{\sum_{i=1}^{n}(y_i - \hat{y}_i)^2}{\sum_{i=1}^{n}(y_i - \bar{y})^2}
\tag{8}
$$

where y_i is the calculated value, $\hat{y}_i$ represents the standard value, and $\bar{y}$ denotes the average of the calculated value [22], [23]. If the calculated value agrees well with the standard value, the R^2 will reach the maximum value of 1. Then the fitting degree between the generated parabolic waveform and standard parabola is shown by Table I and Fig. 4. As one can see, the optimized coefficients of set A are chosen to generate parabolic waveform, and the corresponding R^2 is 0.9991 based on Table I and Fig. 4. Thus, the quality of the generated parabola is acceptable. Of course, we can easily write the optimized expansion of bright parabolic waveform as

$$
\begin{aligned}
T_{bright-pa}(t) = &\, DC + \cos(\omega_m t) - (1/4)\cos(2\omega_m t) \\
&+ (1/9.9)\cos(3\omega_m t) - (1/30)\cos(4\omega_m t).
\end{aligned}
\tag{9}
$$

For dark parabolic waveform generation, the modulation process is illustrated by the case 1 in Fig. 1, and the detailed modulation parameters are shown by Fig. 3. According to Fig. 3(a), once the modulation index is set at 0.725, the coefficient ratio of A/C in (4) is 9.9:1, which is satisfied with the corresponding

TABLE I
THE R-SQUARED (R^2) OF THE PARABOLIC WAVFORM AT DIFFERENT SETS OF
COEFFICIENTS

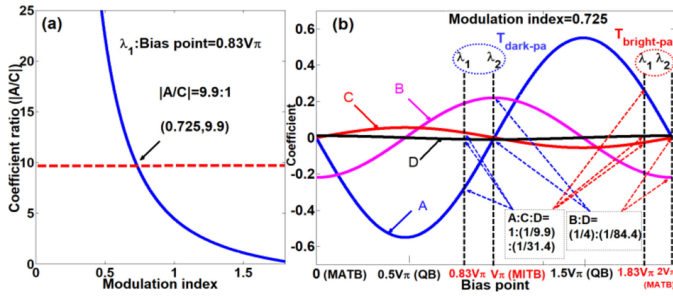| Set of coefficients	First-order	Second-order	Third-order	Fourth-order	R^2
A	1	1/4	1/9.9	1/30	0.9991
B	1	1/4	1/9	1/16	0.9925
C	1	1/4	1/12	1/18	0.9873
D	1	1/4	1/9.5	1/28	0.9987
E	1	1/4	1/13	1/30	0.9941
F	1	1/4	1/7.5	1/20	0.9908
……	……	……	……	……	……

Fig. 3. The calculated values of, (a) The coefficient ratio between the first-order and the third-order harmonic varies with modulation index, (b) The bias point settings for two wavelengths under modulation index of 0.725.

Fig. 4. The comparison between the standard parabola and optimized waveforms with different sets of coefficients.

relationship in (7) or (8). To obtain other required coefficients, as shown in Fig. 3(b), a fixed bias voltage is applied on the MZM to set the bias point at $0.83V_\pi$ for λ_1. At the same time, by tuning the wavelength of λ_2, the bias point for λ_2 reaches V_π (corresponding to MITB). After MZM and demultiplxer, the modulated signal on λ_1 enters the upper branch, and λ_2 goes into the lower branch. In the upper branch, the photocurrent of the modulated signal on λ_1 is

$$i_1(t) \propto DC - \cos(\omega_m t) + (1/1.45)\cos(2\omega_m t) \\ + (1/9.9)\cos(3\omega_m t) - (1/31.4)\cos(4\omega_m t). \quad (10)$$

To approach the (7), the optical field is equally divided into two parts and a relative envelope phase shift of $\pi/2$ (corresponding to ω_m) is introduced between them. After recombining two envelopes again by a polarization beam combiner (PBC), where the PBC is used for preventing optical interference, the photocurrent is written as

$$i_{up}(t) \propto DC + \sin(\omega_m t - \pi/4) + (1/9.9)\sin(3\omega_m t + \pi/4) \\ - (1/22.1)\cos(4\omega_m t). \quad (11)$$

In the lower branch, the optical envelope on λ_2 has phase shift of $\pi/2$ (corresponding to $2\omega_m$) by tuning ODL2, and the corresponding photocurrent can be expressed as

$$i_{low}(t) \propto DC + (1/4)\cos(2\omega_m t + \pi/2) \\ - (1/84.4)\cos(4\omega_m t + \pi). \quad (12)$$
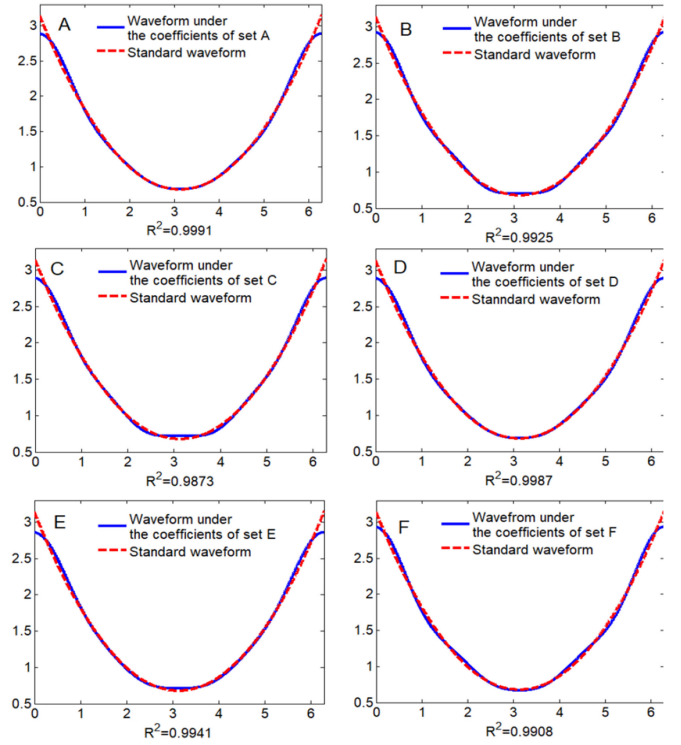
When the $i_{up}(t)$ and $i_{low}(t)$ are overlapped in a PD, the final photocurrent is given by the equation below

$$i(t) = i_{up}(t) + i_{low}(t) \\ = DC + \cos(\omega_m t + 5\pi/4) + (1/4)\cos(2\omega_m t + 10\pi/4) \\ + (1/9.9)\cos(3\omega_m t + 15\pi/4) \\ + (1/30)\cos(4\omega_m t + 20\pi/4) \quad (13)$$

which is equivalent to (7), and the dark parabolic waveform is generated.

To generate bright parabolic waveform, one can keep every step unchanged, but the bias points are set at $1.83V_\pi$ and $2V_\pi$ (MATB) for λ_1 and λ_2 respectively by adjusting the bias voltage and relatively changing their wavelength difference, seen the illustration in Fig. 3(b). The detailed parameters arrangement including $i_{up}(t)$ and $i_{low}(t)$ can be found in the case 2 of Fig. 1, which finally presents a bright parabolic waveform.

B. Sawtooth Waveform

The standard Fourier series expansion of a sawtooth waveform $T_{sa}(t)$ is given by

$$T_{sa}(t) = DC + \sum_{n=1,2,3}^{\infty} \frac{1}{n}\sin(n\omega_m t). \quad (14)$$
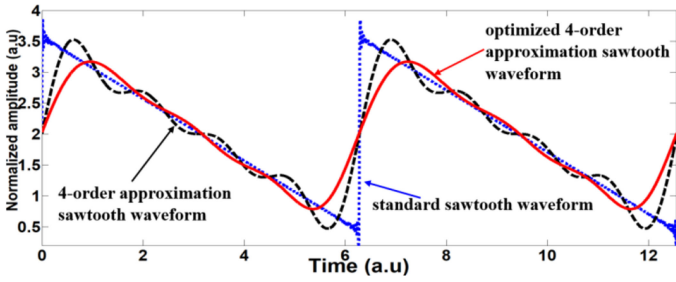
Fig. 5. Comparison results of standard sawtooth, 4th-order approximation sawtooth and optimized 4th-order approximation sawtooth waveform.
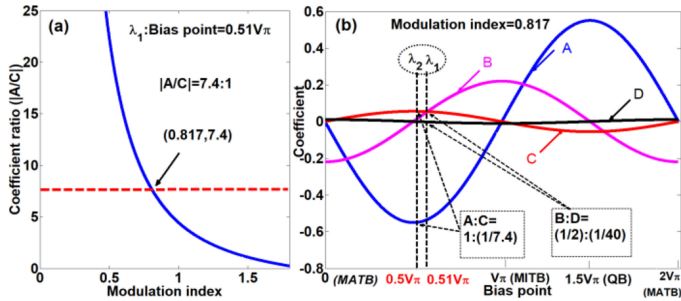

Fig. 6. The calculated values of, (a) The coefficient ratio between the first-order harmonic and the third-order harmonic versus the modulation index, (b) The bias point setting for two wavelengths under modulation index of 0.817.

Under the fourth-order approximation, the optimized expansions of sawtooth and reversed-sawtooth waveform can be written as

$$T_{sa}(t) = DC + \sin(\omega_m t) + (1/2.8)\sin(2\omega_m t) \\ + (1/7.4)\sin(3\omega_m t) + (1/40)\cos(4\omega_m t) \quad (15)$$

and

$$T_{re-sa}(t) = DC + \sin(\omega_m t) - (1/2.8)\sin(2\omega_m t) \\ + (1/7.4)\sin(3\omega_m t) + (1/40)\cos(4\omega_m t) \quad (16)$$

respectively. For comparison, the simulation results are also shown by Fig. 5, which indicates that the linearity and smoothness of the optimized waveform is greatly improved. Under the same quality evaluating process as the parabolic waveform, the corresponding R-squared (R^2) value of 0.8497 for the optimized sawtooth waveform can be obtained. As illustrated by the case 3 in Fig. 1, by setting the bias voltage and wavelength difference, the optical fields of λ_1 and λ_2 are modulated under the bias points at $0.51V_\pi$ and QB (corresponding to the bias point of $0.5V_\pi$) respectively. Meanwhile, the modulation index is equal to 0.817, which determines the concerned coefficient ratios shown by Fig. 6(b). Therefore, the photocurrent of λ_1 and λ_2 are

$$i_1(t) \propto DC - \cos(\omega_m t) + (1/69)\cos(2\omega_m t) \\ + (1/7.4)\cos(3\omega_m t) - (1/987)\cos(4\omega_m t) \quad (17)$$

and

$$i_2(t) \propto DC - \cos(\omega_m t) + (1/7.4)\cos(3\omega_m t). \quad (18)$$

In the upper branch, the optical field is divided and recombined with a relative envelope phase shift of π (corresponding to ω_m). One can obtain the photocurrent of

$$i_{up}(t) \propto DC + (1/2.8)\cos(2\omega_m t) - (1/40)\cos(4\omega_m t). \quad (19)$$

In the lower branch, when the envelope of $i_2(t)$ has a phase shift of $-\pi/4$ (corresponding to ω_m) by tuning ODL2, the photocurrent can be written as

$$i_{low}(t) \propto DC - \cos(\omega_m t - \pi/4) + (1/7.4)\cos(3\omega_m t - 3\pi/4). \quad (20)$$

Then, we can consequently get the total photocurrent after the coupler expressed as

$$i(t) = i_{up}(t) + i_{low}(t) \\ = DC + \sin(\omega_m t + 5\pi/4) + (1/2.8)\sin(2\omega_m t + 10\pi/4) \\ + (1/7.4)\sin(3\omega_m t + 15\pi/4) \\ + (1/40)\cos(4\omega_m t + 20\pi/4) \quad (21)$$

which just presents the expected sawtooth waveform.

Similarly, the reversed-sawtooth waveform can be easily achieved by changing the phase shift in the lower branch from $-\pi/4$ to $-3\pi/4$. This process and calculated results are given by the case 4 in Fig. 1.

C. Frequency Doubling Triangular Waveform

Now, let's consider the Fourier series expansion of a triangular waveform

$$T_{tr}(t) = DC + \sum_{n=1,3,5}^{\infty} \frac{1}{n^2}\cos(n\omega_m t). \quad (22)$$

The first two components can gain good approximation because triangular waveform contains only odd order harmonics and the coefficient values of the higher order components decrease greatly. Therefore, the expansion can be written as

$$T_{tr}(t) = DC + \cos(\omega_m t) + (1/9)\cos(3\omega_m t). \quad (23)$$

Although there are several solutions for triangular frequency doubling triangular waveform generation through external modulation method, frequency doubling triangular waveform generation by using one single-drive MZM is a challenge. Just like the case 5 in Fig. 1, if the MZM with modulation index of 2.508 is biased at MITB for both of λ_1 and λ_2, the modulated signals, as shown by Fig. 7, have no odd order harmonics. In this case, the second-order and the sixth-order harmonics with coefficient ratio of 9:1 (corresponding to B/F in (4)), and the photocurrent of modulated signals on two light fields are

$$i_1(t) = i_2(t) \propto DC + \cos(2\omega_m t) \\ - (1/1.1)\cos(4\omega_m t) + (1/9)\cos(6\omega_m t). \quad (24)$$

In the upper branch, the light field is divided and relatively delayed half period (corresponding to $2\omega_m$). The recombined signal gives a photocurrent of

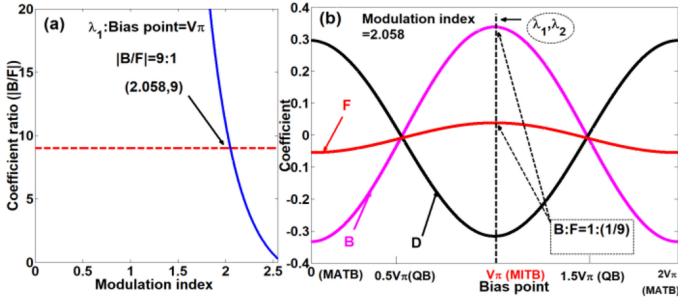$$i_{up}(t) \propto [DC + \cos(2\omega_m t + \pi) - (1/1.1)\cos(4\omega_m t + 2\pi)$$

Fig. 7. The calculated values of, (a) the coefficient ratio between the second-order harmonic and the sixth-order harmonic versus the modulation index, (b) the bias point setting for two wavelengths under modulation index of 2.058.
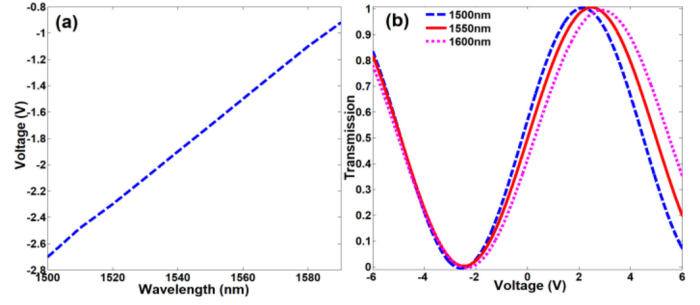

Fig. 8. Measured results. (a) The bias point shift versus the wavelength variation. (b) The transmission characteristics of MZM at different operation wavelengths.

$$+ (1/9)\cos(6\omega_m t + 3\pi)] + [DC + \cos(2\omega_m t)$$
$$- (1/1.1)\cos(4\omega_m t) + (1/9)\cos(6\omega_m t)]$$
$$\propto DC - (1/1.1)\cos(4\omega_m t). \tag{25}$$

Clearly, it presents only the fourth-order harmonic component. In the lower branch, the optical envelope on λ_2 has a phase shift of $\pi/2$ (corresponding to $2\omega_m$) by tuning ODL2. When the envelopes on two branches are overlapped in a PD, the superposition can be expressed as

$$i(t) = i_{up}(t) + i_{low}(t)$$
$$\propto DC + \cos(2\omega_m t + \pi/2) + (1/9)\cos(6\omega_m t + 3\pi/2) \tag{26}$$

which is a frequency doubling triangular waveform. In this case, the corresponding R^2 can reach 0.9977 to contribute an acceptable triangular waveform.

III. EXPERIMENT AND RESULTS

The feasibility of the proposed scheme based on Fig. 1 is experimentally verified. At the beginning, the PD (XPDV210R) response in the wavelength range of 1500 nm to 1620 nm is tested. It has no observable effect on photoelectric conversion with different wavelength. Theoretically, the bias point of a MZM is wavelength dependent, which presents a linear relationship between the bias point shift and wavelength variation. In fact, the transmission function of MZM has minor distortion because the response of the LiNbO$_3$ crystal to different wavelengths is not uniform. Although the distortion is small, it can also be observed in the experiment and has some impact on the experimental parameters selection. In order to understand the results of the experimental parameters selection, the corresponding measurements are given be Fig. 8. The bias shift via wavelength change, as shown by Fig. 8(a), is tested. Fig. 8(a) indicates that the bias point shift has a linear relationship with wavelength variation and a $0.04V_\pi$ (V_π is $5V$ in our case) bias shift corresponds to 10-nm wavelength variation. Fig. 8(b) shows that the MZM transmission characteristics at different operation wavelengths are different. As one can see, the bias point shift via wavelength change decreases along with the longer wavelength, which implies that larger wavelength difference

is required to match the wanted bias point in long wavelength range.

The first demonstration is parabolic waveform generation. Two ECLs emit CWs with wavelengths of 1530.33 nm and 1605.42 nm, which are coupled and modulated by a single-drive MZM with a 4-GHz sinusoidal signal. Under a certain bias voltage, the bias point for 1530.33 nm is at $0.83V_\pi$, and the bias point for 1605.42 nm can reach V_π (corresponding to MITB). Just like the theoretical analysis above, the modulation harmonics on 1530.33 nm has coefficient ratio (A/C) of 9.9:1 by setting modulation index of 0.725, which is satisfied with the (7) or (8). After the demultiplexer, the modulated signals on 1530.33 nm and 1605.42 nm are separated into the upper branch and lower branch, respectively. In the upper branch, the optical is equally divided into two paths by a 3-dB optical coupler, and recombined with a relative envelope phase shift of $\pi/2$. The corresponding electrical spectrum and waveform of the photocurrent (i_{up}) are measured by electrical spectrum analyzer (ESA, Agilent N9010A EXA) and oscilloscope (Osc, Agilent 86100D Infinium DCA-X), which are shown by Fig. 9(a). In the lower branch, the optical envelope has a phase shift of $\pi/2$ by tuning ODL2, whose electrical spectrum and waveform are given by Fig. 9(b). The superposition of these two envelopes is shown by Fig. 9(c) and (d), which is a 4-GHz dark parabolic signal as the theoretical expection.

For bright parabolic waveform generation, the modulation index is still 0.725. The wavelength of ECL 1 remains 1530.33 nm, but it is modulated with bias point at $1.83V_\pi$. At the same time, the wavelength of ECL 2 is tuned to be 1608.42 nm, and the corresponding bias point is shifted to $2V_\pi$ (corresponding to MATB). Then, a bright parabolic waveform can be achieved under the same manipulation processes as the dark signal generation. The measured waveform and electrical spectrum are shown by Fig. 10(a) and (b). To prove the tunability of the system, the frequency of drive signal is changed to be 10 GHz. Parabolic waveforms at 10 GHz are obtained consequently, which are shown by Fig. 10(c) and (d).

Next, the sawtooth and reversed-sawtooth waveforms generation based on the configuration of Fig. 1 are carried out. The ECL 1 and ECL 2 output CWs with wavelengths of 1553.52 nm and 1543.73 nm respectively, which are modulated by a 4-GHz sinusoidal signal with modulation index of 0.817. The bias points
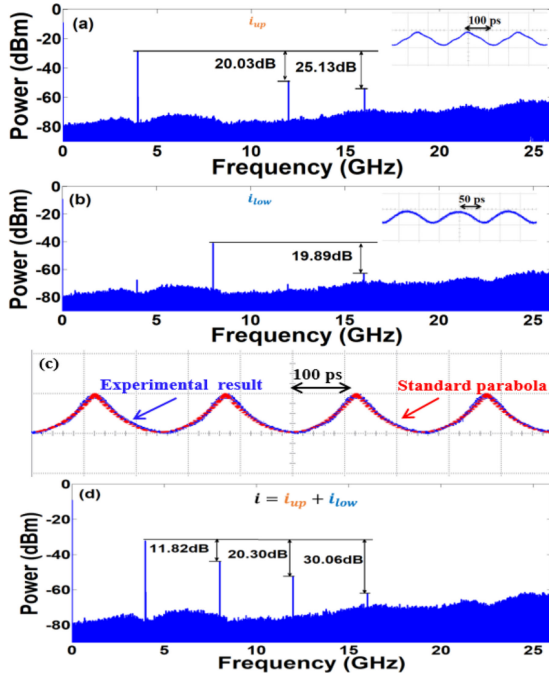
Fig. 9. Measured waveform and electrical spectrum for parabolic waveform generation. (a) Waveform and electrical spectrum of i_{up}. (b) Waveform and electrical spectrum of i_{low}. (c) 4-GHz dark parabolic waveform. (d) The corresponding electrical spectrum of dark parabolic waveform.
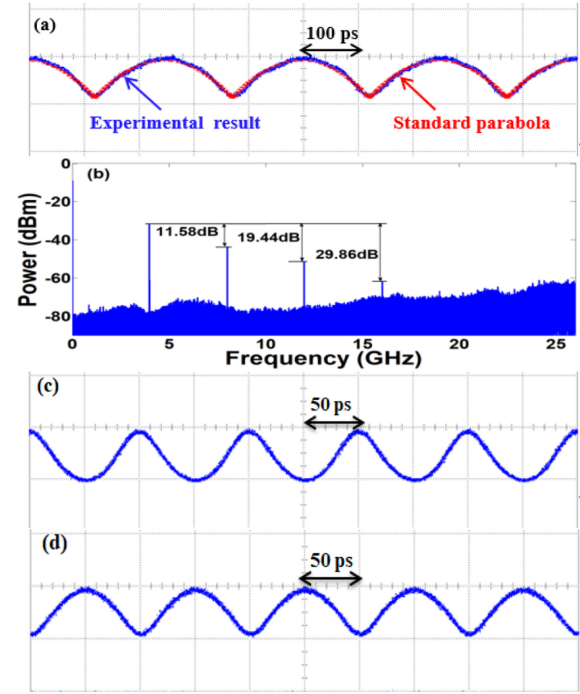

Fig. 10. Experiment results. (a) 4-GHz bright parabolic waveform. (b) The corresponding electrical spectrum. (c) 10-GHz dark parabolic waveform. (d) 10-GHz bright parabolic waveform.

for these two light fields are $0.51V_\pi$ and $0.5V_\pi$ (corresponding to QB). In the upper branch, the signal on 1553.52 nm is divided by a 3-dB optical coupler and recombined with an envelope phase shift of π introduced by OLD1. The measurement of photocurrent (i_{up}) is shown by Fig. 11(a). In the lower branch, the envelope on 1543.73 nm, has a phase shift of $-\pi/4$ by tuning ODL2, as shown by Fig. 11(b). Once the optical envelopes on two branches are overlapped in a PD, the sawtooth signal can be generated, as given by Fig. 11(c) and (d).

Similarly, the reversed-sawtooth waveform can be easily achieved by only changing the envelope phase shift in the lower branch from $-\pi/4$ to $-3\pi/4$, whose waveform and electrical spectrum are given by Fig. 12(a) and (b), sawtooth and reversed-sawtooth waveform with repetition respectively. Fig. 12(c) and (d) show the tunability, where sawtooth and reversed-sawtooth waveform with repetition frequency of 10 GHz are generated under 10-GHz drive signal.

Finally, we show the frequency doubling triangular waveform generation. Two CWs with wavelengths of 1550.07 nm and 1551.62 nm from two ECLs are modulated by a 2-GHz sinusoidal drive signal with modulation index of 2.058. In this case, both of the optical fields are biased at MITB since their wavelengths are close enough. Under these modulation conditions, the photocurrents of modulated signals have coefficient ratio of 9:1 between the second-order and sixth-order harmonic. In the upper branch, the optical field is divided by a 3-dB optical coupler and the optical envelope is relatively delayed half period (corresponding to $2\omega_m$) by tuning ODL1. After recombining, the photocurrent provides just the fourth-order
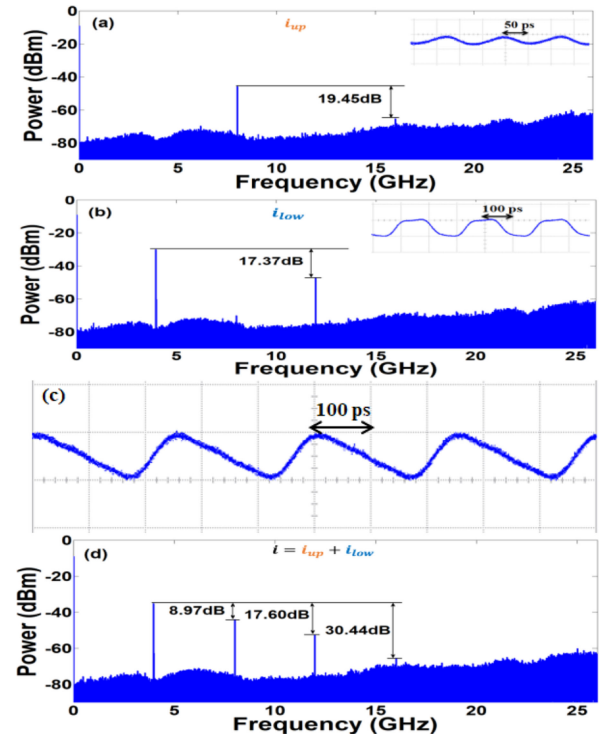
Fig. 11. Measured waveform and electrical spectrum for sawtooth waveform generation. (a) Waveform and electrical spectrum of i_{up}. (b) Waveform and electrical spectrum of i_{low}. (c) 4-GHz sawtooth waveform. (d) The corresponding electrical spectrum of sawtooth waveform.
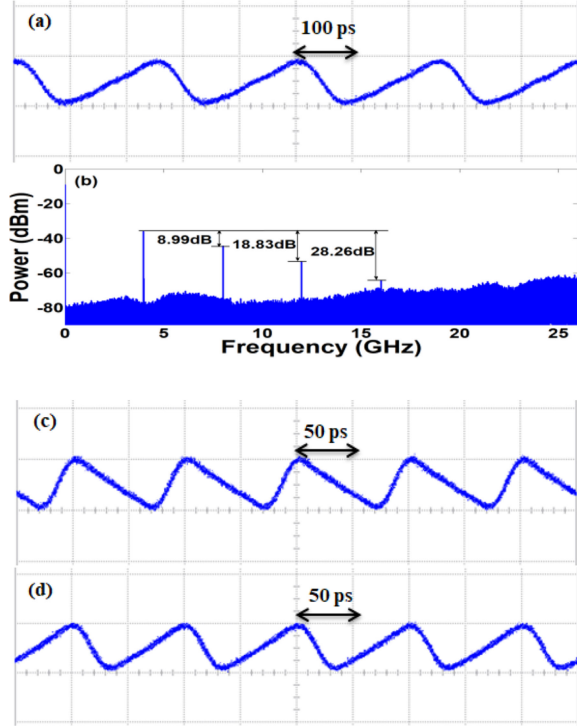
Fig. 12. Experiment results. (a) 4-GHz reversed-sawtooth waveform. (b) The corresponding electrical spectrum. (c) 10-GHz sawtooth waveform. (d) 10-GHz reversed-sawtooth waveform.

harmonic component, as shown by Fig. 13(a). In the lower branch, the optical envelope contains the second, the fourth and the sixth order components with pertinent intensity ratios. After an envelope phase shift of $\pi/2$ (corresponding to $2\omega_m$) by adjusting ODL2, this envelope is overlapped with that of the signal on the upper branch, where the fourth-order components are canceled each other. Therefore, only the second and sixth order components are remained, whose phase and coefficient ratio agree with the Fourier expansion of a frequency doubling triangular waveform. The results are shown by Fig. 13(c) and (d).

Similarly, triangular waveforms at 8 GHz and 10 GHz can be achieved when the frequencies of drive signals are tuned to be 4 GHz and 5 GHz respectively. The corresponding waveforms are given by Fig. 14.

Based on the experimental demonstration above, all results agree with the theoretical analysis well. Therefore, the feasibility of the proposed scheme has been successfully verified. For the system stability, wavelength shift of optical source, polarization variation, optical delay accuracy and temperature are tested and discussed. Firstly, in practice, the wavelength drift of the optical source is a possible factor to influence the stability. Fortunately, a commercial light source usually presents very small wavelength drift. According to Fig. 8, even a wavelength drift of 1nm gives insignificant influence. Secondly, since the MZM is a polarization sensitive device, polarization controller (PC) has to be employed to obtain good modulation efficiency. In our experiment, there is no visible affect caused by polarization variation. Thirdly, an accurate optical delay is required to adjust the phase of envelopes. In our scheme, the optical delay
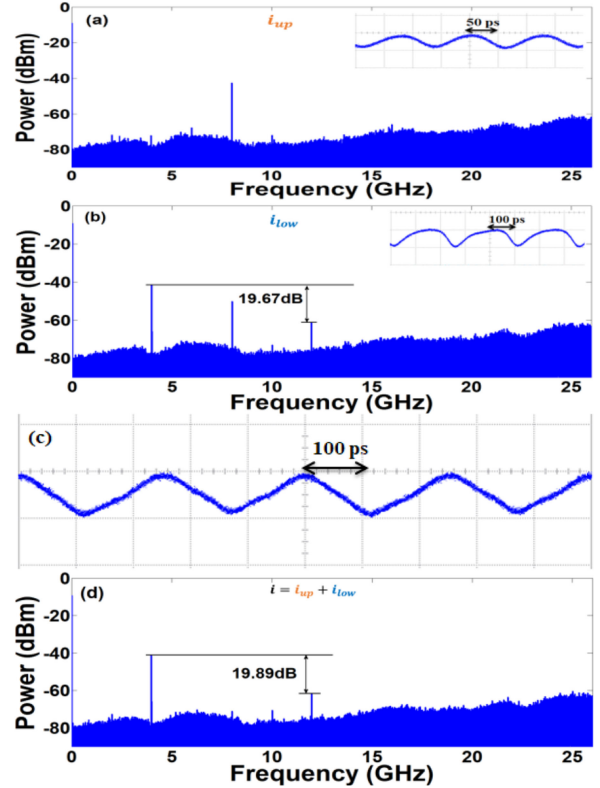

Fig. 13. Measured waveform and electrical spectrum for frequency doubling triangular waveform generation. (a) Waveform and electrical spectrum of i_{up}. (b) Waveform and electrical spectrum of i_{low}. (c) 4-GHz triangular waveform with drive signal of 2 GHz. (d) The corresponding electrical spectrum.
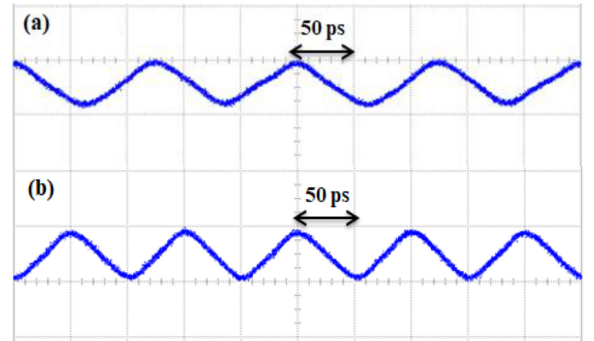

Fig. 14. (a) 8-GHz triangular waveform with drive signal of 4 GHz. (b) 10-GHz triangular waveform with drive signal of 5 GHz.

line (ODL) with 0.05-ps precision and 600-ps tuning range is employed, which is accurate enough for our system. Finally, the affect of DC bias shift with working temperature is also tested. Under a normal laboratory environment, only $2\%V_\pi$ (V_π is 5V in our case) bias shift occurs within 8 hours, which has no observable affect on waveforms generation. Additionally, a table comparing with previous works for system complexity is presented, seen in Table II. Obviously, the modulation technique is a prevalent method to implement waveforms generation. Although different types of modulators are employed in previous works [24]–[28], the single-drive MZM is a good choice due to the lowest requirement on drive signal and bias control as

TABLE II
TYPICAL PHOTONIC METHODS TO GENERATE MICROWAVE WAVEFORM

	Method	Key device	Operation principle	Generated waveform	Advantage	Disadvantage	Reference
1.	Fourier synthesis.	Coherent source; Spatial phase modulator.	Manipulating the amplitude and phase of each spectral line to achieve waveform generation.	Arbitrary waveform.	Accurateness; Various waveform generation.	1. Complex configuration; 2. Susceptible to environmental perturbation.	[1]
2.	External modulation technique.	One LD; One MZM; One optical filter.	Strictly controlling modulation tones as well as assistant filtering.	Triangular waveform.	Simple devices.	1. Strict requirement on optical filter; 2. Only triangular waveform generation.	[24]
		One LD; One polarization modulator; One optical filter.		Square waveform; Triangular waveform; Sawtooth waveform.	Three fundamental waveforms generation.	Strict requirement on optical filer.	[25]
		One LD; One DD-MZM; Chromatic dispersion.	Strictly controlling modulation tones.	Short pulses; Flat-top pulses; triangular pulses; Sawtooth pulses.	Four types of pulse generation.	1. Two different drive signals; 2. Two biases adjustment; 3. Chromatic dispersion control.	[26]
		One LD; One DD-MZM.		Triangular waveform; Square waveform.	Compactness.	1. Two different drive signals; 2. Two bias adjustments; 3. Two fundamental waveforms generation only.	[13]
		One LD; One DP-MZM.		Triangular waveform.	Compactness.	1. Three independent bias adjustments; 2. Triangular waveform generation only.	[10]
		One LD; One DP-MZM.		Gaussian pulses; Trapezoidal pulses; Triangular pulses; Sawtooth pulses; Sinc pulses.	Five types of waveforms generation.	1.Two different drive signals; 2.Three independent bias adjustments.	[27]
3.	Time-domain synthesis.	One LD; One Dual Polarization-MZM.	Strictly controlling modulation tones and overlapping optical envelope.	Triangular waveform; Square waveform; Sawtooth waveform.	Three fundamental waveforms generation.	1. Peculiar device with two drive signals; 2 .Polarization sensitivity.	[28]
Our scheme	Comprehensive utilization of Fourier synthesis and Time-domain synthesis.	Two LDs; One MZM.	The wavelength-dependent bias effect in MZM.	Parabolic waveform, Sawtooth waveform, Frequency doubling triangular waveform.	1. Basic simple commercial devices without matching filtering; 2. Three types of waveforms generation, including some challenging waveforms generation, e.g. parabolic waveform and frequency doubling triangular waveform.	One more tunable LD required.

well as the cost. Of course, the advanced modulators, such as DD-MZM or DP-MZM, may have more compact configuration, but the modulation parameters are relatively complicated. In our scheme, one more tunable LD is employed, but the potential of wavelength-dependent bias shift is greatly exploited, which extends the ability of harmonics generation within one MZM.

IV. CONCLUSION

In conclusion, a method of tunable arbitrary waveform generation based on one single-drive MZM and two optical carriers is proposed, in which the characteristic of wavelength-dependent bias shift of a MZM is utilized. By properly arranging the bias voltage and wavelengths, two sets of modulation components are generated on two optical fields, which can be independently manipulated and finally synthesize the desired waveforms. Theoretically, the operation conditions for parabolic waveform, sawtooth waveform and frequency doubling triangular waveform generation are analyzed and simulated. In the experiment, the expected waveforms are successfully generated, which agree with the theoretical results well. The significance of this scheme is that the harmonics generation ability in a MZM can be extended by the wavelength-dependent bias effect, which is beneficial to flexible waveform generation. In addition, it also presents the advantages of simple structure, low cost and full use of the bandwidth.

REFERENCES

[1] A. I. Latkin, S. Boscolo, R. S. Bhamber, and S. K. Turitsyn, "Optical frequency conversion, pulse compression and signal copying using triangular pulses," in *Proc. 34th Eur. Conf. Opt. Commun.*, Brussels, Belgium, 2008, pp. 1–2.

[2] J. P. Yao, "Microwave photonics," *J. Lightw. Technol.*, vol. 27, no. 3, pp. 314–335, Feb. 2009.

[3] J. P. Yao, "Photonic generation of microwave arbitrary waveforms," *Opt. Commun.*, vol. 284, no. 15, pp. 3723–3736, 2011.

[4] S. T. Cundiff and A. M. Weiner, "Optical arbitrary waveform generation," *Nat. Photon.*, vol. 4, no. 11, pp. 760–766, 2010.

[5] Z. Jiang, C. B. Huang, D. E. Leaird, and A. M. Weiner, "Optical arbitrary waveform processing of more than 100 spectral comb lines," *Nat. Photon.*, vol. 1, no. 8, pp. 463–467, 2007.

[6] Y. T. He *et al.*, "Photonic microwave waveforms generation based on two cascaded single-drive Mach–Zehnder modulators," *Opt. Exp.*, vol. 26, no. 6, pp. 7829–7841, 2018.

[7] W. Li, W. T. Wang, and N. H. Zhu, "Photonic generation of radio-frequency waveforms based on dual-parallel Mach–Zehnder modulator," *IEEE Photon. J.*, vol. 6, no. 3, Jun. 2014, Art. no. 5500608.

[8] J. Li, X. Zhang, B. Hraimel, T. Ning, L. Pei, and K. Wu, "Performance analysis of a photonic-assisted periodic triangular-shaped pulses generator," *J. Lightw. Technol.*, vol. 30, no. 11, pp. 1617–1624, Jun. 2012.

[9] J. Li *et al.*, "Photonic-assisted periodic triangular-shaped pulses generation with tunable repetition rate," *IEEE Photon. Technol. Lett.*, vol. 25, no. 10, pp. 952–954, May 2013.

[10] F. Z. Zhang, X. Z. Ge, and S. L. Pan, "Triangular pulse generation using a dual-parallel Mach–Zehnder modulator driven by a single-frequency radio frequency signal," *Opt. Lett.*, vol. 38, no. 21, pp. 4491–4493, 2013.

[11] N. K. Fontaine *et al.*, "32 phase X32 amplitude optical arbitrary waveform generation," *Opt. Lett.*, vol. 32, no. 7, pp. 865–867, 2007.

[12] Y. Jiang *et al.*, "Photonic microwave waveforms generation based on time-domain processing," *Opt. Exp.*, vol. 23, no. 15, pp. 19442–19452, 2015.

[13] J. J. Hu, J. Li, J. Y. Zhao, Z. C. Ren, Y. Y. Gu, and M. S. Zhao, "A simple scheme for photonic generation of microwave waveforms using a dual-drive Mach–Zehnder modulator," *Appl. Sci-Basel.*, vol. 10, no. 21, pp. 2076–3417, 2020.

[14] G. F. Bai, L. Hu, Y. Jiang, Y. J. Zi, T. W. Wu, and F. Q. Huang, "Versatile photonic microwave waveforms generation using a dual-parallel Mach–Zehnder modulator without other dispersive elements," *Opt. Commun.*, vol. 396, pp. 134–140, 2017.

[15] Y. Jiang *et al.*, "Photonic generation of triangular waveform by utilizing time-domain synthesis," *IEEE Photon. Technol. Lett.*, vol. 27, no. 16, pp. 1725–1728, Aug. 2015.

[16] R. Wang, Y. Jiang, C. Wei, and H. F. Liu, "Parabolic pulse generation based on a multiply operation of two triangular pulses," *Opt. Eng.*, vol. 59, no. 10, 2020, Art. no. 100502.

[17] Y. Xia *et al.*, " Photonic microwave waveforms generation based on pulse caring and superposition in time-domain," *Opt. Commun.*, vol. 414, pp. 177–184, 2018.

[18] X. Liu *et al.*, "Photonic generation of triangular-shaped microwave pluses using SBS-based optical carrier processing," *J. Lightw. Technol.*, vol. 32, no. 20, pp. 3797–3802, Oct. 2014.

[19] T. W. Wu, C. F. Zhang, H. Zhou, H. S. Huang, and K. Qiu, "Photonic microwave waveforms generation based on frequency and time-domain synthesis," *IEEE Access*, vol. 6, pp. 34327–34379, 2018.

[20] C. Wei *et al.*, "Tunable microwave sawtooth waveform generation based on one single-drive Mach–Zehnder modulator," *Opt. Exp.*, vol. 28, no. 6, pp. 8098–8107, 2020.

[21] S. Dubovitsky, W. H. Steier, and S. Yegnanarayanan, and B. Jalali, "Analysis of improvement of Mach–Zehnder modulator linearity performance for chirped and tunable optical carriers," *J. Lightw. Technol.*, vol. 20, no. 5, pp. 886–891, May 2002.

[22] T. Tjur, "Coefficients of determination in logistic regression models a new proposal: The coefficient of discrimination," *Amer. Statist.*, vol. 63, no. 5, pp. 366–372, 2009.

[23] E. Kasuya, "On the use of r and r squared in correlation and regression," *Ecol. Res.*, vol. 34, no. 1, pp. 235–236, 2019.

[24] J. Li *et al.*, "Photonic-assisted periodic triangular-shaped pulses generation with tunable repetition rate," *IEEE Photon. Technol. Lett.*, vol. 25, no. 10, pp. 952–954, May 2013.

[25] W. Liu and J. Yao, "Photonic generation of microwave waveforms based on a polarization modulator in a Sagnac loop," *J. Lightw. Technol.*, vol. 32, no. 20, pp. 3637–3644, Oct. 2014.

[26] D. Bo, Z. Gao, W. Xu, H. Chen, and N. Wada, "Generation of versatile waveforms from cw light using a dual-drive Mach-Zehnder modulator and employing chromatic dispersion," *J. Lightw. Technol.*, vol. 31, no. 1, pp. 145–151, Jan. 2013.

[27] J. Yan, Z. Xia, S. Zhang, M. Bai, and Z. Zheng, "A flexible waveforms generator based on a single dual-parallel Mach–Zehnder modulator," *Opt. Commun.*, vol. 334, pp. 31–34, Jan. 2015.

[28] F. Zhang, B. Gao, and S. Pan, "Time-domain waveform synthesis using a dual-polarization modulator," *IEEE Photon. Technol. Lett.*, vol. 28, no. 23, pp. 2689–2692, Dec. 2016.